

See discussions, stats, and author profiles for this publication at: <https://www.researchgate.net/publication/279279240>

Effects of Oxide Contact Layer on the Preparation and Properties of $\text{CH}_3\text{NH}_3\text{PbI}_3$ for Perovskite Solar Cell Application

ARTICLE *in* THE JOURNAL OF PHYSICAL CHEMISTRY C · JUNE 2015

Impact Factor: 4.77 · DOI: 10.1021/acs.jpcc.5b02984

CITATIONS

2

READS

79

2 AUTHORS:



Jie Zhang

Chimie ParisTech

6 PUBLICATIONS 19 CITATIONS

[SEE PROFILE](#)



Thierry Pauperté

Chimie ParisTech

163 PUBLICATIONS 4,724 CITATIONS

[SEE PROFILE](#)

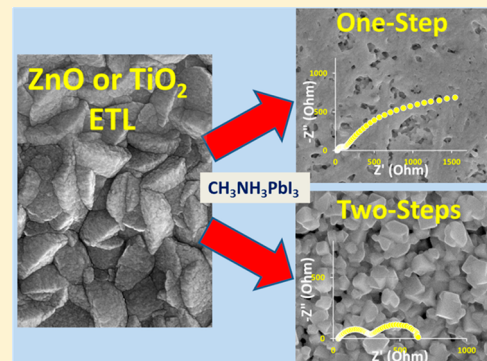
Effects of Oxide Contact Layer on the Preparation and Properties of $\text{CH}_3\text{NH}_3\text{PbI}_3$ for Perovskite Solar Cell Application

Jie Zhang and Thierry Pauporté*

PSL Research University, Chimie ParisTech – CNRS, Institut de Recherche de Chimie Paris, UMR8247, 11 rue P. et M. Curie, 75005 Paris, France

Supporting Information

ABSTRACT: In perovskite solar cells, oxide electron transport layers (ETL) and their interface with the organometal trihalides are key to achieve efficient and stable devices. In the present work we investigate ZnO and TiO_2 ETLs and their influence on the preparation of $\text{CH}_3\text{NH}_3\text{PbI}_3$ film by two different techniques. In the “one-step” technique, a solution is used for the deposition of a precursor layer which is dripped and subsequently annealed. In the “two-step” sequential technique, a PbI_2 precursor layer is converted into perovskite. We show that, on ZnO , the annealing treatment of the “one-step” deposited layer is optimum for a duration time of only 2 min. This duration is much less critical for the TiO_2 underlayer. Long annealing times produce the degradation of the pigment and formation of PbI_2 . It is also shown that the “one-step” technique gives better results for the sensitization of smooth oxide underlayers whereas the “two-step” one must be utilized for rough or structured underlayer sensitization. The best solar cell performances were achieved by combining a low-overvoltage electrodeposited ZnO layer, a planar architecture, and a perovskite layer prepared by a “one-step” deposition-dripping route. A maximum overall conversion efficiency of 15% was measured for the ZnO -based perovskite solar cell. Cell impedance spectra have been measured over a large applied voltage range. Their analysis, using an ad-hoc equivalent circuit, shows that charge recombinations are reduced for the “one-step” perovskite and that a better interface with the oxide is produced in that case.



1. INTRODUCTION

Very recently, perovskite-based solar cells (PSCs) have emerged as the most promising new generation of photovoltaic technology.^{1–17} Although perovskite (PE) materials have been known since the 19th century, the interest in the use of perovskite as the active light absorbing material in a solar cell is much more recent. Methylammonium lead halide compounds were used for the first time as a sensitizer in a liquid-electrolyte analog of a dye-sensitized solar cell in 2009.¹ In 2012, PSC emerged as a high efficiency technology candidate by replacing the liquid electrolyte by a solid organic molecular glass and by improving the technique for depositing the perovskite layer.^{3,4} The perovskite materials used are hybrid organic–inorganic compounds with a 3D crystal structure of general formula ABX_3 (with $\text{A} = \text{CH}_3\text{NH}_3$, $\text{B} = \text{Pb(II)}$ and $\text{X} = \text{Cl, Br, or I}$). In the cell, the organolead trihalide compound, which is a direct bandgap semiconductor, acts as the solar light absorber in which excitons are photogenerated. The electron–hole charge collection is ensured by the selective contacts with two adjacent phases that generate the driving force for the charge separation. The electrons are transferred to the conduction band of a material layer forming the electron transport layer (ETL), and the holes are transferred to a hole transport material (HTM), usually an organic molecular glass. The hybrid perovskite can be prepared by using either vapor phase deposition⁵ or solution

processing techniques.^{6,9,10} Among the latter, two processes have been shown promising. In the first one, the precursors, dissolved in an ad-hoc solvent, are spin-coated to prepare a precursor layer. This layer is subsequently annealed to obtain the desired product.^{2,3,9,10,16} On the other hand, Burschka et al.⁶ have developed a sequential two-step technique in which a layer of lead halide is first deposited. This layer is subsequently transformed into the perovskite by exposing it to a solution of methylammonium halide.

Currently, most state-of-the art PSCs utilize planar TiO_2 layers or mesoscopic TiO_2 scaffold layers on top of a compact titania layer to provide a substrate on which the perovskite can be grown.⁹ The preparation of these layers requires annealing and sintering processes at high temperature, typically 500 °C. On the other hand, other inorganic or organic materials have been used for the application, such as phenyl-C61-butyric acid methyl ester (PCBM)^{15,16} or ZnO .^{13,14,17–25} One of the challenges is to process ETL at low temperature to reduce the production cost and for the preparation of flexible lightweight devices on plastic substrates. ZnO is a wide bandgap semiconductor with electron affinity similar to that of TiO_2 .

Received: March 28, 2015

Revised: June 8, 2015

Published: June 10, 2015



ACS Publications

© 2015 American Chemical Society

14919

DOI: 10.1021/acs.jpcc.5b02984
J. Phys. Chem. C 2015, 119, 14919–14928

It can be grown by various techniques with high structural quality at low temperature.^{26–28} Moreover, the conductivity of ZnO is several orders of magnitude higher than that of TiO₂, which makes it favor electron transport toward the back contact.^{29,30} It is therefore a viable alternative to TiO₂ for the PSC application.^{13,14,17–25} Kelly et al.²⁰ have reported remarkably high efficiency PSCs using a thin layer of dense planar ZnO prepared by spin-coating. On the other hand, our group has shown that electrodeposition is a promising technique for the low temperature preparation of ZnO ETL for PSC application.^{13,14}

It appears that the ETL and its interface with the organometal trihalide are keys to get efficient and stable cells. The ETL not only receives and transports the electronic charges, it also influences the sensitization through three aspects: the perovskite layer morphology and loading, which depend on the structure and roughness of the ETL, the quality of the ETL/perovskite interface, and the quality of the perovskite itself, since the ETL intervenes in the full precursor conversion into perovskite. In the present work, we have investigated the effect of oxide wide bandgap semiconductor chemical nature and structure on the preparation of either “one-step” or “two-step” CH₃NH₃PbI₃ films. ZnO layers have been investigated and compared to TiO₂ mesoscopic reference layers. The perovskite films have been characterized for various annealing times. The heterostructures have been included in solar cells, and the best efficiency has been achieved for a planar device architecture that combines an electrodeposited ZnO ETL and a one-step CH₃NH₃PbI₃ layer. We have clearly established that the one-step process gives rise to better quality perovskite films and interfaces with reduced recombination side reactions.

2. EXPERIMENTAL SECTION

2.1. Preparation of the layers. Three different oxide layers have been investigated in the present work for the electron transport and selective contact. The ZnO layers were prepared directly on cleaned fluorine-doped tin oxide (FTO) coated glass substrate (TEC-10) in a three-electrode cell. It was rotated at 145 rpm upon the deposition process. The counter-electrode was a zinc wire, and the applied potential was controlled versus a saturated calomel reference electrode (SCE). The deposition bath was a solution of Zn(NO₃)₂ at a concentration of 0.08 M dissolved in Milli-Q quality water (18.2 MΩ·cm) maintained at 60 °C. The deposition was performed at a constant applied voltage of −1.15 V/SCE for 120 s (layer hereafter noted i-ZnO-120s) or −0.9 V/SCE for 420 s (layer hereafter noted i-ZnO-420s).

The mesoscopic nanoparticle TiO₂ films (noted np-TiO₂) were prepared by the spin-coating technique. The FTO coated glass substrates (TEC10) were cleaned with soap, sonicated with acetone and ethanol for 5 min each, and rinsed with distilled water. They were then etched in 10% HCl for 5 min in an ultrasonic bath. The TiO₂ blocking layer (noted BL-TiO₂) was deposited by spin-coating at 2000 rpm for 30 s a 0.15 M titanium diisopropoxidebis(acetylacetone) in 1-butanol solution. The layer was subsequently heated at 125 °C on a hot plate for 5 min. The same process was repeated twice with a 0.3 M titanium diisopropoxidebis(acetylacetone) in 1-butanol. This BL was finally heated at 500 °C for 15 min in a furnace.³ After cooling down, the substrate was treated in a 0.04 M aqueous solution of TiCl₄ for 30 min at 70 °C, rinsed with water, and annealed at 500 °C for 20 min. The mesoporous

TiO₂ composed of 18-nm-sized particles was prepared by spin-coating at 5000 rpm for 30 s a TiO₂ paste (Dyesol 18NR-T diluted in ethanol with a 2:7 weight ratio). After drying at 125 °C for 10 min, the TiO₂ film was gradually heated to 500 °C for 15 min.⁶

We have investigated two procedures for CH₃NH₃PbI₃ perovskite preparation. In the hereafter called “one-step” technique, a precursor solution with a concentration of 45 wt % was produced by mixing CH₃NH₃I (0.2 g) and PbI₂ (0.578 g) in N,N-dimethylformamide (1 mL) and stirring at room temperature for 20 min.¹⁰ CH₃NH₃I was synthesized according to ref 8. The CH₃NH₃PbI₃ solution (60 μL) was dropped on the ZnO or TiO₂ layer, and the substrate was then two-step spun at 1000 rpm for 5 s and at 2500 rpm for 25 s. After 21 s, 150 μL of chlorobenzene was dropped on the center of the substrate. Beforehand, these spin-coating parameters were optimized using i-ZnO. The perovskite layer was subsequently annealed on a hot plate at 100 °C for various duration times.

In the hereafter called “two-step” sequential deposition technique, 70 μL of PbI₂ solution heated at 70 °C (dissolved in N,N-dimethylformamide at a concentration of 460 mg·mL^{−1}) was spin-coated on top of the ZnO or TiO₂ layer at 3,000 rpm for 15 s. This step was repeated once. After drying at 70 °C for 30 min in air in an oven, the substrate was dipped into a solution of CH₃NH₃I in 2-propanol (10 mg·mL^{−1}) and then dried at 70 °C for various duration times.

2.2. Thin film characterizations. The film thicknesses were measured with a Dektak 6 M stylus profilometer equipped with a 12.5 μm tip. The sample morphologies were examined with a high resolution Ultra 55 Zeiss FEG scanning electron microscope (FE-SEM) at an acceleration voltage of 10 kV. The film structure was characterized with a Phillips X-Pert high-resolution X-ray diffractometer (XRD) operated at 40 kV and 45 mA and using Cu Kα radiation with λ = 1.5406 Å. The film total transmissions and total reflections were measured with a Cary 5000 UV-vis-NIR spectrophotometer equipped with an integrating sphere. The absorbance spectra were calculated from these two parameters. The photoluminescence measurement system combined a YAG:Nd laser and a HR250 monochromator (Jobin-Yvon) coupled to a UV-enhanced intensified charge-coupled device (ICCD; Roper). The excitation wavelength was 266 nm. Raman scattering spectra were measured at room temperature with a Renishaw INVIA apparatus equipped with a microscope and a CCD detector. A 532 nm solid-state green laser was used for off-resonance excitation with 50 mW power. The instrument was calibrated using a silicon standard.

2.3. Solar cell preparation and characterizations. The spiro-OMeTAD-based hole-transport layer was deposited using a solution containing 80 mg of spiro-OMeTAD, 28.5 μL of 4-tertbutylpyridine, and 17.5 μL of lithium bis-(trifluoromethanesulfonyl)imide (Li-TFSI) (520 mg of Li-TFSI in 1 mL of acetonitrile) all dissolved in 1 mL of chlorobenzene. This precursor solution was deposited by spin-coating at 2,000 rpm for 15 s.²⁰ Finally, a 100-nm-thick silver layer was deposited by thermal evaporation on the Spiro-OMeTAD layer as a back contact.

The I–V curves were recorded by a Keithley 2400 digital source meter, using a 0.15 V·s^{−1} voltage sweep rate in the negative scan direction. The solar cells were illuminated with a solar simulator (Abet Technology Sun 2000) filtered to mimic AM 1.5G conditions. The illuminated surface was delimited by a black mask with an aperture diameter of 3 mm. The power

density was calibrated to $100 \text{ mW} \cdot \text{cm}^{-2}$ by the use of a reference silicon solar cell. The impedance spectra were measured under 0.95–1 sun illumination provided by a Schott lamp, between 600 kHz and 0.12 Hz, using a Solartron FRA1255 frequency response analyzer coupled with a PAR273 EGG potentiostat. The AC signal was 20 mV.

3. RESULTS AND DISCUSSION

3.1. Oxide layer preparation and characterizations.

One of the objectives of the present work was to compare ZnO and TiO₂ layers as selective contact semiconductor materials in perovskite solar cells and to investigate the oxide layer role in the CH₃NH₃PbI₃ preparation and properties. The i-ZnO-120s layers were electrodeposited at 60 °C, applying a constant voltage of −1.15 V/SCE for 120 s. On the other hand, the i-ZnO-420s layers were prepared by applying a voltage of −0.9 V/SCE for 420 s. Figure 1 shows the variation of the deposition

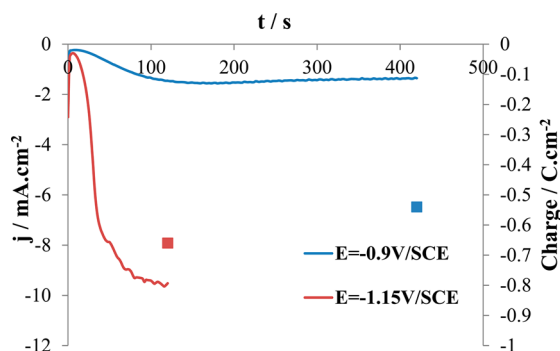


Figure 1. Variation of the current density (lines) as a function of ZnO deposition time and total electrical charge density exchanged (dots) for two deposition potentials.

current density with time for the two different layers. The measured current is due to the electrochemical reduction reaction of nitrate ions.^{31,32} The reaction generates nitrites and hydroxide ions and ZnO is precipitated by the chemical reaction of the zinc and hydroxide ions at the electrode surface. In both cases, the starting current is low and increases with time before reaching a plateau. This is due to the progressive covering of the FTO substrate by ZnO. The plateau is reached when the substrate is fully covered by the deposit. In Figure 1 and Table 1, the total charge density exchanged after the layer deposition completion is also presented.

The SEM images of the ZnO deposited films are shown in Figure 2a–c. The i-ZnO-420s layer is uniform and pinhole-free, covers the entire substrate, and is made of large grains (Figure 2a). The cross-sectional view (Figure 2a inset) shows a flat

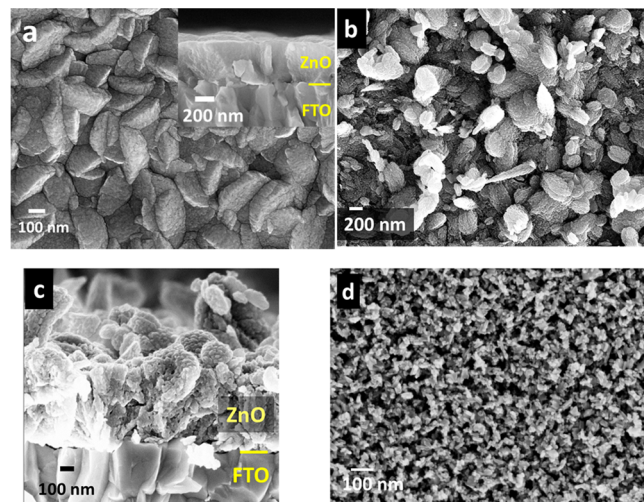


Figure 2. FE-SEM images. Top views of (a) i-ZnO-420s layer, (b) i-ZnO-120s layer, and (d) np-TiO₂ layer. Cross-sectional views of (a inset) i-ZnO-420s layer and (c) i-ZnO-120s layer.

ZnO surface. The R_{rms} roughness measured by profilometry is equal to 31 nm, and the mean layer thickness is 420 nm (Table 1). The i-ZnO-120s layer is made of large grains that fully cover the FTO substrate (Figure 2b). On the cross-sectional view (Figure 2c), some protruding ZnO grains emerge from the layer. The R_{rms} roughness is measured at 65 nm by profilometry (Table 1). Close inspection of the grain surface shows no crystal facets but ten-nanometer-sized asperities (Figure 2b). Moreover, the cross-sectional view (Figure 2c) exhibits the presence of pinholes in the grains. Figure 2d shows a top view of the mesoscopic nanoparticle TiO₂ layer. In most of the literature on perovskite solar cells, TiO₂ is used as the ETL, and we have studied TiO₂ for the sake of comparison. The layers were made of sintered nanoparticles that covered the TiO₂ BL. Their mean thickness was 280 nm, and the surface was flat with a R_{rms} , measured by profilometry, of 30 nm (Table 1).

The crystalline structure of the layers was revealed by X-ray diffraction (XRD) measurements, and the patterns are shown in Figure 3a. The electrodeposited layers are made of well-crystallized ZnO with the wurtzite hexagonal structure. On the other hand, the diffraction peaks for the tetragonal phase of the anatase TiO₂ layer are very weak due to the thinness of the TiO₂ layer. Figure 3b shows the Raman spectra of the oxide layers. For i-ZnO-420s and i-ZnO-120s, the dominant peaks are found at 100 and 438 cm^{-1} and attributed to the low- E_2 and high- E_2 modes, respectively, of nonpolar optical phonons.³³ The tetragonal anatase TiO₂ phase is characterized by six Raman active modes $A_{1g} + 2B_{1g} + 3E_g$.³⁴ In Figure 3b, the

Table 1. Characteristics of ZnO and TiO₂ Films Used As Electron Transport Layers

sample	Applied potential	$Q^a / \text{C} \cdot \text{cm}^{-2}$	Calculated thickness ^b /nm	Measured thickness/nm	$R_{\text{rms}}^c / \text{nm}$	$\lambda^d / \text{eV} (\text{nm})$	E_g^e / eV	$R_{\text{rms}}^f / \text{nm}$
i-ZnO-420s	−0.9 V	0.54	406	420	31	3.28 (378)	3.33(d)	19
i-ZnO-120s	−1.15 V	0.66	496	750	65	3.32 (374)	3.36(d)	80
np-TiO ₂				280	30	2.61 (475)	3.30(i)	20

^a Q , the electrical charge density exchanged during the electrodeposition process. ^b Obtained from the measured total electrical charge exchanged, see Figure 1, as $D (\mu\text{m}) = (Q/nF)(MW/\rho) = 0.7519Q (\text{C} \cdot \text{cm}^{-2})$, with n the number of electrons exchanged in the electrochemical reaction ($n = 2$), F the Faraday constant ($96 \cdot 485 \text{ C} \cdot \text{mol}^{-1}$), MW the molar weight of ZnO ($81.4 \text{ g} \cdot \text{mol}^{-1}$) and ρ the density of ZnO ($5.61 \text{ g} \cdot \text{cm}^{-3}$). ^c Root mean square of roughness (rms) measured by profilometry using a $12.5 \mu\text{m}$ tip. ^d Near-Band edge ZnO UV photoemission and TiO₂ defect emission energy (wavelength). ^e Measured from the transmittance and reflectance spectra for a direct optical bandgap (d) and for an indirect one (i). ^f After two-step perovskite layer deposition.

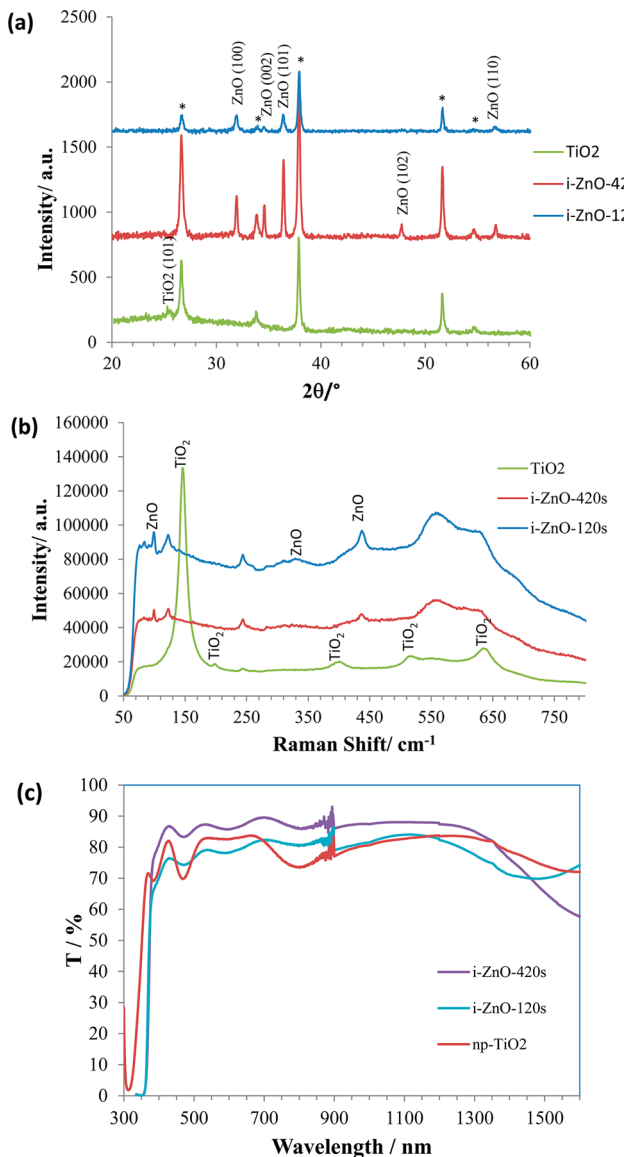


Figure 3. (a) XRD patterns of i-ZnO and TiO₂ layers. (b) Raman spectra of i-ZnO layers and TiO₂ layer. (c) Total optical transmittance of i-ZnO and TiO₂ layers.

typical anatase TiO₂ peaks at 147 cm⁻¹ (E_g), 202 cm⁻¹ (E_g), 406 cm⁻¹ (B_{1g}), 520 cm⁻¹ (A_{1g}, B_{1g}), and 638 cm⁻¹ (E_g) are observed.³⁵

The oxide layer optical properties are presented in Figure 3c, and the i-ZnO-420s layer as well as the np-TiO₂ layer show a high transmittance in the visible-near IR region. The i-ZnO-120s transmittance was lower due to the higher roughness and light scattering. The optical absorption edges of the films were analyzed to determine the oxide optical bandgaps (noted E_g) in Figure S1 (Supporting Information) and are gathered in Table 1. The photoluminescence (PL) of the ZnO and TiO₂ layers is shown in Figure S1c (Supporting Information). The ZnO PL spectra are characterized by a strong UV near band-edge emission and a weak visible emission. Compared to i-ZnO-420s, the UV emission peak for the i-ZnO-120s has a little blue shift. The UV to visible emission intensity ratio is much higher for i-ZnO-420s compared to i-ZnO-120s. It shows the better structural quality of the former sample. This is due to the lower overvoltage used for the deposition. It gives rise to a slower

growth rate and then to a better structural quality of the oxide material. The excitonic emission of the anatase TiO₂ is not observed due to the indirect bandgap, and the emission spectrum is characterized by a blue emission centered at 475 nm (Figure S1c, inset).

3.2. Effect of oxide substrate on one-step perovskite preparation. The ZnO and TiO₂ layers described above have been used as substrate for the preparation of CH₃NH₃PbI₃ layers. The two main techniques used in the literature to yield high efficiency solar cells, namely a one-step and a two-step sequential technique described in the experimental section, have been investigated.

In the one-step process, the annealing is performed on a hot plate at 100 °C. We have followed the changes induced by this treatment on the precursor layer. In the case of either i-ZnO-120s or i-ZnO-420s substrate, a metachromism phenomenon was observed. The initial film, which is a mixture of CH₃NH₃I, PbI₂, and solvent, had a shiny gray color (Figure 4a). After 1 min of annealing, the solvent was evaporated and CH₃NH₃PbI₃ was formed. The color changed to dark-brown. For an annealing time of more than 10 min the color gradually became yellow. The film was full yellow-colored after an annealing time of 40 min. These changes have been further characterized by XRD measurements in Figure 4b. After 1 min of annealing time, the diffractogram peaks are indexed by CH₃NH₃PbI₃, ZnO, and SnO₂. After more than 2 min, an additional peak is found at 12.72° assigned to the (001) reflection of the 2H polytype of PbI₂ (JCPDS card no. 00-007-0235). With increasing annealing time, this PbI₂ peak increased in intensity and those related to CH₃NH₃PbI₃ decreased. We also noted the appearance of peaks at 25.96°, 39.63°, and 52.29° assigned to PbI₂(101), PbI₂(110), and PbI₂(004), respectively. A fast degradation of the perovskite layer deposited on ZnO and heated at 100 °C is observed. The sample noted “2 days” was stored in a dry place during this time. Some darkening was observed that suggests some partial reverse reaction and perovskite reformation. We have noted that this metachromism sequence was observed for annealing either in air or in the dry nitrogen-purged atmosphere of a glovebox. Therefore, this degradation reaction does not require oxygen or water.

A different behavior was found for the one-step perovskite deposited on a TiO₂ substrate layer (Figure 5). We found that the precursor spin-coated on TiO₂ was homogeneously shiny gray-colored. The film color changed to dark brown upon the first annealing minute (Figure 5a). Then after, there was no color change upon the first 40 min. One had to anneal for 8 h the layer to observe a yellowish tinge appearance. In the XRD patterns in Figure 5b, no new phase appeared upon the first 40 min of annealing time. For the 8 h annealing time, a peak assigned to PbI₂(101) is present. We conclude that the degradation of one-step CH₃NH₃PbI₃ occurs very slowly upon heating when anatase TiO₂ is the substrate.

According to the previous results, 2 min was chosen for the annealing time of one-step perovskite layers. SEM pictures in Figure 6a–c show the aspect of the resulting layers on various selective contact underlayers. The perovskite layer is made of ribbon-like structures that fully cover the i-ZnO-420s underlayer. High-magnification views show that the film is composed of merged grains with a 100–200 nm size (Figure 6a inset). The perovskite layer is less covering on the i-ZnO-120s underlayer, and pinholes are observed (Figure 6b). The layer is also rougher. The morphological characteristics of the ZnO

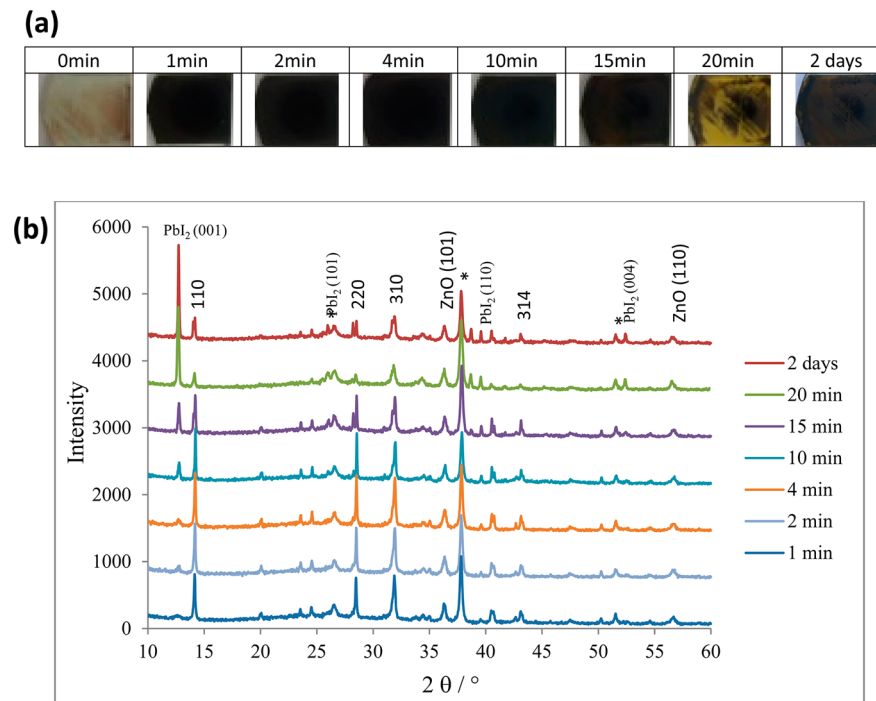


Figure 4. (a) Images of one-step perovskite layers deposited on i-ZnO-120s with increasing annealing time at 100 °C. The sample “2 days” was stored for 2 days after an annealing treatment of 20 min. (b) XRD patterns of the layers presented in (a).

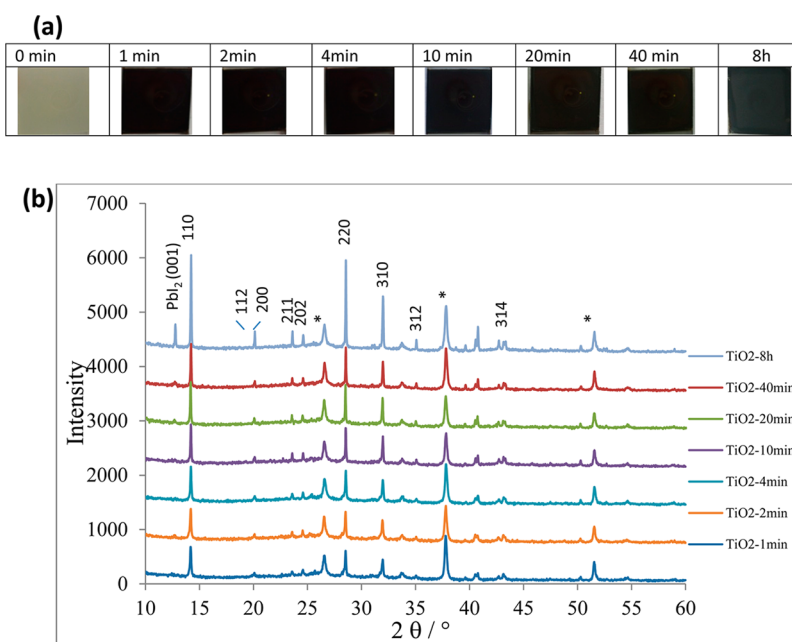
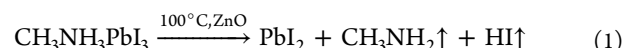


Figure 5. (a) Images of one-step perovskite layers deposited on np-TiO₂ upon annealing for various times. (b) XRD pattern of the layers presented in (a).

underlayer influence the coverage of the perovskite film. On TiO₂ substrate, the ribbon structures are also found as for the flat i-ZnO-420s but with a lower density (Figure 6c). A consequence is a higher hole density. High magnification views show that the ribbons are composed of merged grains with a 100–150 nm size.

We have clearly shown a different behavior of the perovskite upon annealing at 100 °C with the substrate oxide material. CH₃NH₃PbI₃ is quite stable on TiO₂, and the XRD pattern did not significantly change upon the first 40 min of annealing time.

On the other hand, in the case of ZnO, the perovskite annealing must be very short to avoid its decomposition and PbI₂ formation. The decomposition reaction is catalyzed by the ZnO underlayer and can be written:



Methylamine and hydroiodic acid are volatile compounds at 100 °C, and they are eliminated. PbI₂ remains on the ZnO surface and crystallizes.

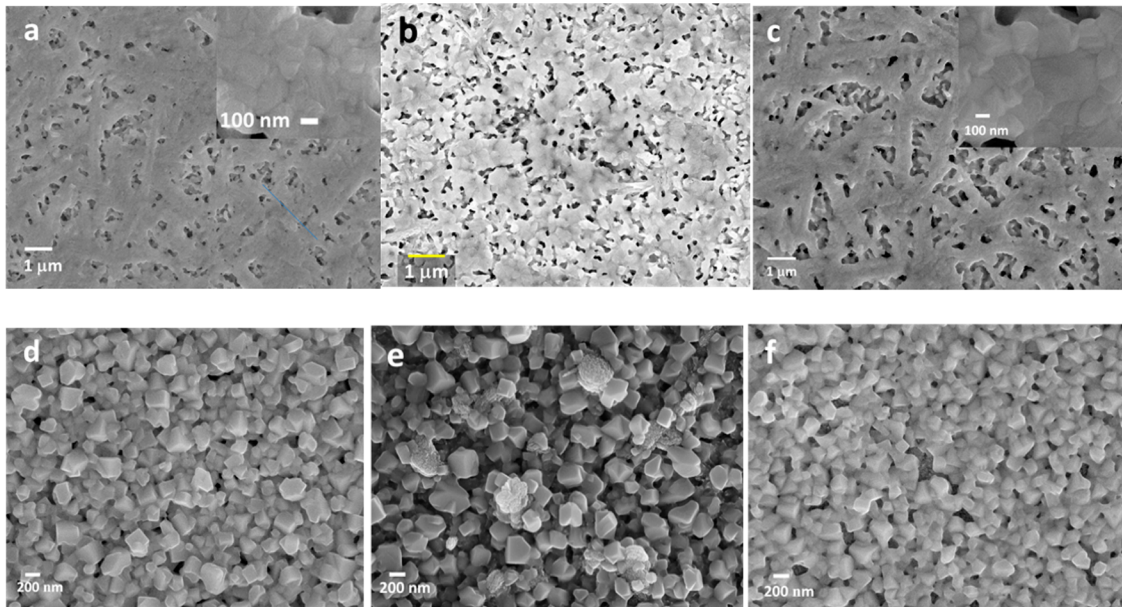


Figure 6. (a–c) SEM top-views of one-step $\text{CH}_3\text{NH}_3\text{PbI}_3$ sensitized: (a) i-ZnO-420s, (b) i-ZnO-120s, and (c) np-TiO₂. High magnification views are shown as insets in (a) and (c). (d–f) SEM top-views of two-step $\text{CH}_3\text{NH}_3\text{PbI}_3$ sensitized: (d) i-ZnO-420s, (e) i-ZnO-120s, and (f) np-TiO₂.

3.3. Effect of oxide substrate on two-step perovskite preparation. The other technique widely employed in the literature for the preparation of $\text{CH}_3\text{NH}_3\text{PbI}_3$ is the two-step sequential route described first by Burshka et al.⁶ In this technique a PbI_2 layer is first deposited on the oxide substrate by spin-coating⁶ or evaporation²⁴ and subsequently transformed into perovskite pigment by a dipping treatment in a solution of $\text{CH}_3\text{NH}_3\text{I}$. The layer is finally annealed. We tested the perovskite stability upon the annealing treatment at 70 °C in an oven for ZnO and TiO₂ underlayers. After drying with argon (0 min), the layer had the dark-brown color typical of perovskite (Figure 7a). $\text{CH}_3\text{NH}_3\text{PbI}_3$ was detected by XRD mixed with a smaller peak that can be assigned to PbI_2 (001) (Figure 7b) and would be the signature of the presence of unreacted precursor. This result is in agreement with other

papers which describe the presence of this diffraction peak.²⁴ The layer color was unchanged after an annealing time of 10 or 30 min, and the XRD patterns remained the same (Figure 7). The behavior was not different in the case of TiO₂. The same color and XRD patterns were found in the case of the TiO₂ underlayer (Figure S2, Supporting Information). These results show that, at the 70 °C annealing temperature used, the prepared perovskite is stable either on ZnO or on TiO₂ underlayers.

Figures 6d–f are SEM top-views of the layers. The two-step route layers are made of a closely packed collection of blocklike perovskite crystallites. The layer on i-ZnO-420s is rather smooth and homogeneous, and it fully covers the ZnO (Figure 6d). The grain size ranges between 150 and 250 nm, and the perovskite layer is smoother than the ZnO underlayer (Table 1). The perovskite layer roughness is higher in the case of i-ZnO-120s (Table 1) due to the roughness of the ZnO underlayer and the presence of protruding grains. In this case, the R_{rms} of the perovskite layer is higher than the initial ZnO one (80 nm R_{rms}). The perovskite layer is smooth on TiO₂ (Table 1) and made of smaller grains (120–200 nm) compared to ZnO. A close image inspection shows some gaps between the perovskite grains and regions of TiO₂ are uncovered by the pigment.

3.4. Optical properties of the heterostructures. The heterostructure optical properties have been characterized by absorption measurements. The spectra displayed in Figure 8a present a clear absorption edge at about 800 nm. The direct bandgap for the perovskite prepared by the two different routes is the same, measured at 1.59 eV (Figure S3, Supporting Information). Figure 8a clearly shows a different absorbance behavior for the one-step and the two-step prepared materials. The one-step layer absorbs homogeneously below 620 nm. We can note that i-ZnO-120s/ $\text{CH}_3\text{NH}_3\text{PbI}_3$, which is the rougher sample, absorbs more sunlight due to a higher pigment loading. There is a striking difference in the absorbance curve shape for the two-step perovskite. For this material, two absorption edges are observed, namely the perovskite band-to-band transition

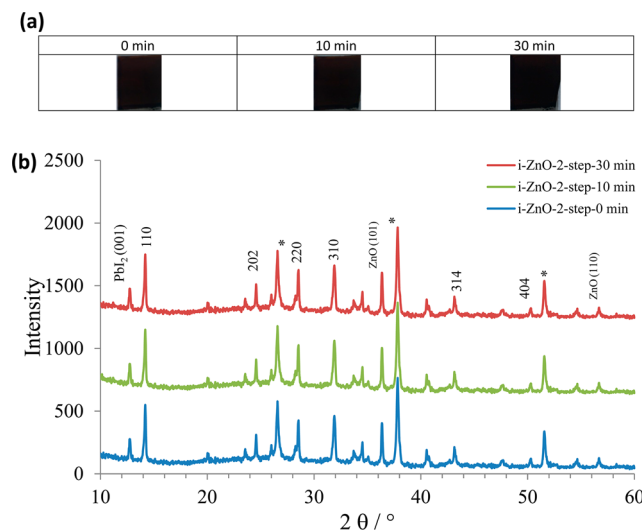


Figure 7. (a) Images of two-step perovskite layers deposited on i-ZnO-120s substrate for various annealing times. (b) XRD patterns of the layers presented in (a).

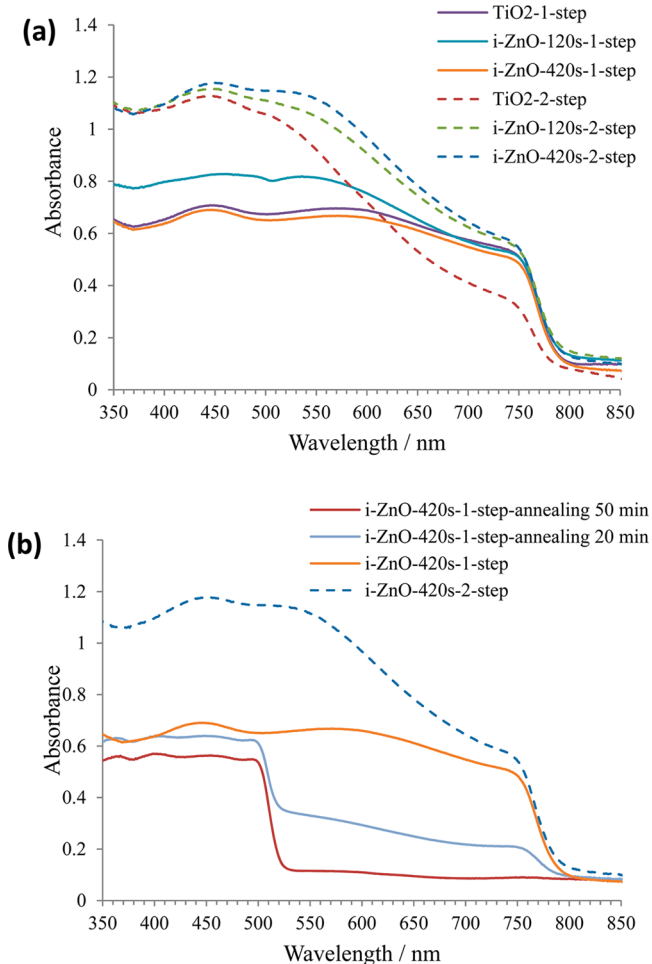


Figure 8. (a) Absorbance spectra of one-step and two-step $\text{CH}_3\text{NH}_3\text{PbI}_3$ layers deposited on ZnO and TiO₂ underlayers. (b) Absorbance spectra of a one-step $\text{CH}_3\text{NH}_3\text{PbI}_3$ layer deposited on ZnO annealed for 2 min, 20 min, and 50 min at 100 °C. The dashed line is the absorbance of the two-step perovskite deposited on the same substrate.

edge at about 800 nm and a diffuse edge between 700 and 550 nm. The two-step pigment layers have a higher absorbance, especially below 700 nm, for the three studied oxide underlayers. A striking feature of the two-step perovskite absorbance curves in Figure 8a is that the adsorption edge of the direct transition in PbI₂, which should be localized at 520 nm, is not observed. This is a puzzling result because in the XRD pattern of Figure 7b, diffraction peaks that can be indexed by the hexagonal PbI₂ structure are found, but on the other hand, the direct band-to-band absorption of PbI₂ is not observed. This point remains to be clarified in a future work.

In Figure 8b, we have followed the absorbance of the one-step layer deposited on ZnO upon annealing at 100 °C. After 20 min, the absorption edge of PbI₂ is clearly observed in this case. It is combined with the $\text{CH}_3\text{NH}_3\text{PbI}_3$ edge whose amplitude is reduced. After 50 min of annealing time, the absorption spectrum is attributable to a pure PbI₂ layer. The analysis of the edge in Figure S4 gives a direct bandgap of 2.4 eV in agreement with the value reported for this material in the literature. This confirms the occurrence of the proposed reaction (eq 1).

3.5. Effect of ETL and perovskite preparation route on the solar cell performances.

Solar cells have been prepared

by spin-coating the doped SpiroOMeTAD as a hole transport layer. A silver back contact was finally evaporated on the top of this layer. The effects of the oxide layer and of the perovskite preparation technique on the cell performances have been investigated. $I-V$ curves are presented in Figure 9a,b, and the

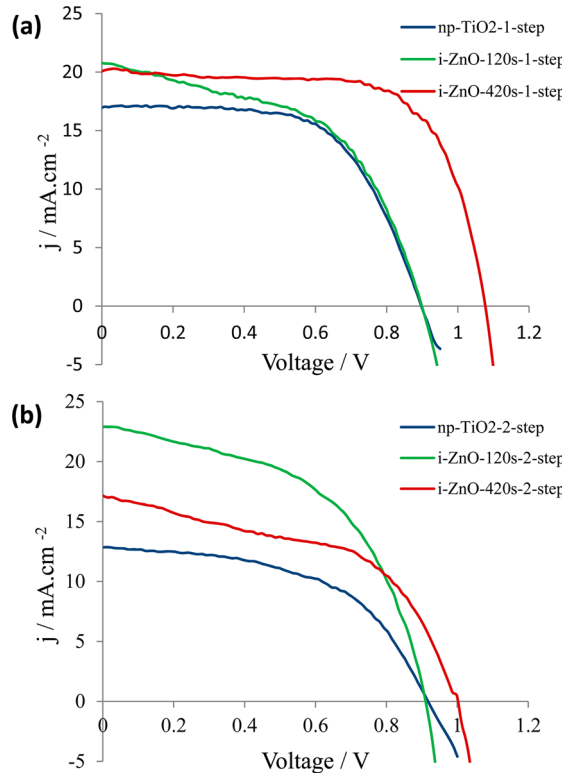


Figure 9. (a) $I-V$ curves of one-step perovskite and (b) two-step perovskite solar cells prepared using various oxide underlayers.

Table 2. Effect of Perovskite Preparation Route and Selective Contact Material on $I-V$ Curve Characteristics (AM1.5G, 100 mW·cm⁻²)

Oxide layer	Perovskite	V_{oc}/V	$J_{sc}/\text{mA}\cdot\text{cm}^{-2}$	FF/%	PCE/%
i-ZnO-420s	One-step	1.08	20.04	69.47	14.99
	Two-step	0.99	17.08	51.99	8.83
i-ZnO-120s	One-step	0.90	20.67	52.28	9.71
	Two step	0.91	22.60	52.90	10.91
np-TiO ₂	One-step	0.90	16.98	61.90	9.43
	Two-step	0.92	12.84	53.05	6.25
BL-TiO ₂ ^a	One-step	0.64	18.64	56.44	6.68
	Two-step	0.79	12.98	36.83	3.76

^aCell prepared using the TiO₂ blocking layer as the oxide selective contact.

cell characteristics are gathered in Table 2. The best-performing cells were obtained using i-ZnO-420s as ETL and the one-step route for $\text{CH}_3\text{NH}_3\text{PbI}_3$ sensitizer preparation. The cell cross-section view shows that, in this case, a planar architecture is obtained (Figure S5, Supporting Information). The power conversion efficiency achieved a remarkable 15% value. We have demonstrated that electrodeposition is a relevant technique for the preparation of efficient ETLs for high performance cells. We note that i-ZnO-420s gives a better V_{oc}

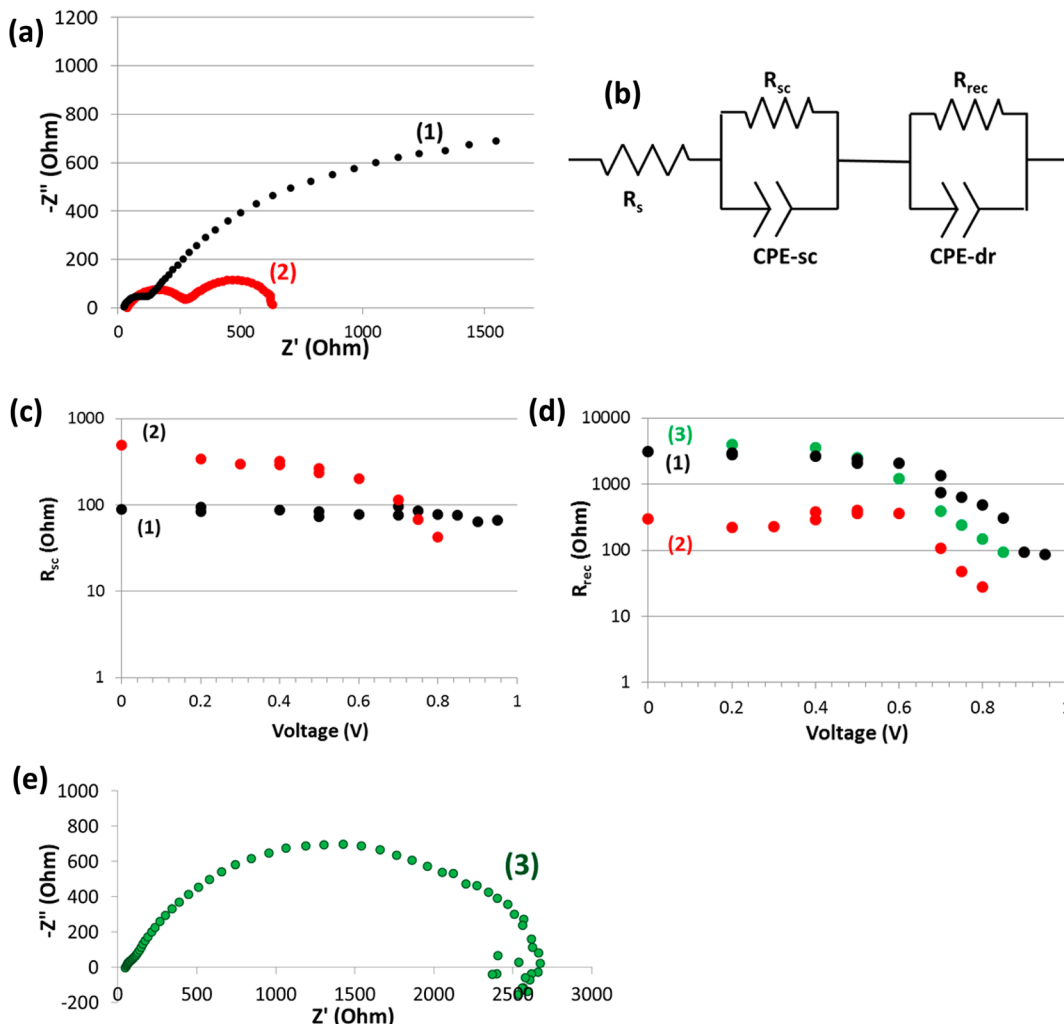


Figure 10. (a,e) Impedance spectra measured at 0.5 V, (b) equivalent electrical circuit used for fitting the data, (c) variation of R_{sc} with applied voltage, and (d) variation of R_{rec} with the applied voltage. (1) i-ZnO-420s/one-step perovskite solar cell; (2) i-ZnO-120s/two-step perovskite solar cell, (3) i-ZnO-120s/one-step perovskite solar cell.

(1.08 V) compared to i-ZnO-120s and np-TiO₂. Globally, for the flatter oxide sublayers, namely i-ZnO-420s, BL-TiO₂, and np-TiO₂, the best efficiency was achieved with the one-step route, which produces smooth covering capping layers (Figure 6a–c). On the other hand, for the oxide layers with a marked relief and protruding grains, the two-step route is better suited and ensures a better coverage of these structures. We can note that in the case of the flatter oxide films the fill factor can be significantly enlarged when the one-step perovskite is used. Values higher than 60% could be achieved whereas with the two-step technique the FF values we obtained were in the 52–53% range and below. In Table 2, the best J_{sc} was measured for the rough i-ZnO-120s/two-step CH₃NH₃PbI₃, in good agreement with the large light absorbance measured for this heterostructure in Figure 8a. The IPCE curves shown in Figure S6 confirm the better quantum efficiency in the visible region due to a higher light harvesting for the two-step sensitized cell. The effect of the I – V curve scan direction on the photovoltaic parameters is displayed in Table S1 (Supporting Information). An hysteresis is observed for all the investigated cells. The smaller hysteresis is recorded for the i-ZnO-120s/two-step CH₃NH₃PbI₃ device. However, no systematic effect of

the perovskite preparation route on the amplitude of the hysteresis is noted.

The best solar cells prepared with the one-step and two-step perovskite have been investigated by impedance spectroscopy under illumination and over a large applied voltage range. Typical Nyquist plots of the spectra are presented in Figure 10a. The spectra have been fitted with the equivalent electrical circuit presented in Figure 10b.^{14,36} This circuit is composed of a series resistance, R_s , due to the contacts and FTO layers. The high frequency loop is modeled by a R_{sc} //CPE-sc circuit. R_{sc} is a resistance due to the selective contacts, and CPE-sc is related to interfacial capacitances with frequency dispersion. The low frequency loop is assigned to the recombination due to perovskite and is fitted by the R_{rec} //CPE-dr circuit. The CPE is a constant phase element which takes into account the dispersion of the perovskite dielectric relaxation capacitance.^{14,37,38}

R_{sc} is plotted as a function of the applied voltage in Figure 10c. Different behavior is found for the two cells. It steeply decreases in the case of the two-step perovskite whereas the decrease is slow for the one-step one. Moreover, R_{sc} is higher for the two-step cell over most of the applied voltage range investigated. This explains the lower FF for the two-step cell

because R_{sc} contributes to the total series resistance.¹⁴ The different behavior between the two cells, which have a Spiro-OMeTAD layer with about the same characteristics, suggests that the contribution of the HTL in the resistance is negligible. R_{sc} is mainly due to the oxide layer resistance and to the resistance of charge transfer between the perovskite and the oxide layer.

Figure 10d shows the variation of R_{rec} with the applied voltage. Higher R_{rec} values are found for the one-step cell. We can conclude that the recombinations are less in the one-step perovskite due to a better quality of the material interfaces. For both perovskite routes, R_{rec} slowly decreases or is almost constant at low voltage. Above a certain voltage threshold, R_{rec} decreases markedly. The recombination side reaction is promoted by applying high voltage, and the total current decreases. The higher threshold voltage and R_{rec} for the i-ZnO-420s/one-step solar cells explain their high open circuit voltage.

The impedance spectra of the i-ZnO-120s/one-step solar cell are presented in Figure 10e and in Figure S7. The shape is different and looks like the spectra of perovskite solar cells measured in the dark. No clear high frequency loop could be analyzed. The spectra are dominated by an arc of a circle in the high–middle frequency range. At low frequency, an additional loop is found with a positive imaginary part due to a negative capacitance. The resistance of the middle frequency range loop has been extracted and is presented in Figure 10d. Its behavior and order of magnitude are the same as for the i-ZnO-420s/one-step perovskite cell. This resistance is then attributed to the recombination and is plotted in Figure 10d. R_{rec} decreases more rapidly for an i-ZnO-120s cell compared to an i-ZnO-420s cell, and consequently, the cell V_{oc} is significantly lower for the former compared to the latter (Table 2).

4. CONCLUSIONS

In conclusion, we have investigated the effect of the oxide ETL underlayer and perovskite preparation route on the sensitizer layer characteristics and on the solar cell performances and electrical properties. ZnO layers with a planar 2D geometry and ZnO layers with some roughness and protruding grains have been investigated. They have been compared to nanoparticle TiO₂ and flat TiO₂ barrier layer films. We show that the oxide underlayer has a marked influence on the one-step perovskite preparation. CH₃NH₃PbI₃ is degraded to form PbI₂ after several minutes of annealing at 100 °C. The same process has been observed in the case of TiO₂ underlayer but with a much slower kinetics. ZnO catalyzes the degradation at 100 °C, and the optimized annealing time was found to be 2 min. In the case of the two-step route, the annealing is performed at lower temperature, and the perovskite layer is not degraded. The XRD patterns of two step perovskite show the presence of peaks that can be assigned to unreacted PbI₂. However, the absorbance spectra of the obtained product do not show the presence of a PbI₂ direct transition at 520 nm but a diffuse absorbance edge. The two-step route gives rise to more absorbing layers than the one-step route, especially in the green-blue wavelength region, which is globally beneficial for solar light harvesting.

The best performances were achieved by combining a low-overvoltage electrodeposited ZnO layer, a planar architecture, and a perovskite layer prepared by a one-step deposition-dripping route. A maximum overall conversion efficiency of about 15% was measured. Globally, for the flatter oxide sublayers, namely i-ZnO-420s, BL-TiO₂, and np-TiO₂, the best

efficiency was achieved with the one-step CH₃NH₃PbI₃ synthetic route because it results in a quite smooth perovskite coating. On the other hand, the two-step route is more suitable for rough or structured (nanorods, ...) ¹³ underlayers because the technique ensures a better coverage of these structures. The investigation of the cells by impedance spectroscopy has shown that the one-step perovskite gives rise to a material in which the charge recombinations are reduced compared to the two-step material. Moreover, our investigations suggest that a better oxide–perovskite interface is created and that the interfacial resistance is consequently reduced. These results are promising since the best cell is prepared at low temperature, and this opens the gate to the fabrication of flexible solar cells on plastic substrate. More work is ongoing to improve the one-step perovskite layer compactness and covering and to produce larger grains to reduce, to a greater extent, bulk defects and grain boundaries. This should improve the charge carrier mobility and limit the recombination phenomena.

■ ASSOCIATED CONTENT

■ Supporting Information

Determination of ZnO and TiO₂ layer optical bandgaps. Photoluminescence spectra of ZnO and TiO₂ layers. Effect of annealing time on two-step perovskite prepared on TiO₂ substrate. Optical bandgap determination of perovskite layers. Direct optical bandgap determination of perovskite degradation product. SEM cross-sectional view of the planar i-ZnO-420s/one-step perovskite solar cell. IPCE curves of the cells. $I-V$ characteristics for the two scan directions. Impedance spectra of i-ZnO-120s/two-step CH₃NH₃PbI₃ solar cell at various applied voltages. The Supporting Information is available free of charge on the ACS Publications website at DOI: 10.1021/acs.jpcc.Sb02984.

■ AUTHOR INFORMATION

Corresponding Author

*E-mail: thierry.pauporte@chimie-paristech.fr. Tel.: (331) 55 42 63 83.

Notes

The authors declare no competing financial interest.

■ ACKNOWLEDGMENTS

J.Z. acknowledges the Guangzhou Government for a scholarship (Oversea Study Program of the Guangzhou Elite Project). We thank P. Aschehoug and Dr. B. Viana (IRCP-Paris, France) for photoluminescence measurements.

■ REFERENCES

- Kojima, A.; Teshima, K.; Shirai, Y.; Miyasaka, T. Organometal Halide Perovskites as Visible-Light Sensitizers for Photovoltaic Cells. *J. Am. Chem. Soc.* **2009**, *131*, 6050–6051.
- Im, J. H.; Lee, C. R.; Lee, J. W.; Park, S. W.; Park, N. G. 6.5% Efficient Perovskite Quantum-Dot-Sensitized Solar Cell. *Nanoscale* **2011**, *3*, 4088–4093.
- Kim, H. S.; Lee, C. R.; Im, J. H.; Lee, K. H.; Moehl, T.; Marchioro, A.; Moon, S. J.; Humphry-Baker, R.; Yum, J. H.; Moser, J. E.; et al. M. Lead Iodide Perovskite Sensitized All-Solid-State Submicron Thin Film Mesoscopic Solar Cell with Efficiency Exceeding 9%. *Sci. Rep.* **2012**, *2*, 591.
- Lee, M. M.; Teuscher, J.; Miyasaka, T.; Murakami, T. N.; Snaith, H. J. Efficient Hybrid Solar Cells Based on Meso-Superstructured Organo-Metal Halide Perovskite. *Science* **2012**, *338*, 643–647.

- (5) Liu, M.; Johnston, M. B.; Snaith, H. J. Efficient Planar Heterojunction Perovskite Solar Cells by Vapour Deposition. *Nature* **2013**, *501*, 395–398.
- (6) Burschka, J.; Pellet, N.; Moon, S. J.; Humphy-Baker, R.; Gao, P.; Nazeeruddin, M. K.; Grätzel, M. Sequential Deposition as a Route to High-Performance Perovskite-Sensitized Solar Cells. *Nature* **2013**, *499*, 316–319.
- (7) Docampo, P.; Ball, J. M.; Darwich, M.; Eperon, G. E.; Snaith, H. J. Efficient Organometal Trihalide Perovskite Planar-Heterojunction Solar Cells on Flexible Polymer Substrates. *Nat. Commun.* **2013**, *4*, 2761.
- (8) Etgar, L.; Gao, P.; Xue, Z. S.; Peng, Q.; Chandiran, A. K.; Liu, B.; Nazeeruddin, M. K.; Grätzel, M. Mesoscopic $\text{CH}_3\text{NH}_3\text{PbI}_3/\text{TiO}_2$ Heterojunction Solar Cells. *J. Am. Chem. Soc.* **2012**, *134*, 17396–17399.
- (9) Jeon, N. J.; Noh, J. H.; Kim, Y. C.; Yang, W. S.; Ryu, S.; Seok, S. I. Solvent Engineering for High-Performance Inorganic-Organic Hybrid Perovskite Solar Cells. *Nat. Mater.* **2014**, *13*, 897–903.
- (10) Xiao, M.; Huang, F. Z.; Huang, W. C.; Dkhissi, Y.; Zhu, Y.; Etheridge, J.; Gray-Weale, A.; Bach, U.; Cheng, Y. B.; Spiccia, L. A. Fast Deposition-Crystallization Procedure for Highly Efficient Lead Iodide Perovskite Thin-Film Solar Cells. *Angew. Chem., Int. Ed.* **2014**, *53*, 9898–9903.
- (11) Mei, A. Y.; Li, X.; Liu, L. F.; Ku, Z. L.; Liu, T. F.; Rong, Y. G.; Xu, M.; Hu, M.; Chen, J. Z.; Yang, Y. A Hole-Conductor-Free, Fully Printable Mesoscopic Perovskite Solar Cell with High Stability. *Science* **2014**, *345*, 295–298.
- (12) Zhou, H. P.; Chen, Q.; Li, G.; Luo, S.; Song, T. B.; Duan, H. S.; Hong, Z. R.; You, J. B.; Liu, Y. S.; Yang, Y. Interface Engineering of Highly Efficient Perovskite Solar Cells. *Science* **2014**, *345*, 542–546.
- (13) Zhang, J.; Barboux, P.; Pauporté, T. Electrochemical Design of Nanostructured ZnO Charge Carrier Layers for Efficient Solid-State Perovskite-Sensitized Solar Cells. *Adv. Energy Mater.* **2014**, *4*, 1400932.
- (14) Zhang, J.; Juárez-Pérez, E. J.; Mora-Seró, I.; Viana, B.; Pauporté, T. Fast and Low Temperature Growth of Electron Transport Layers for Efficient Perovskite Solar Cells. *J. Mater. Chem. A* **2015**, *3*, 4909–4915.
- (15) Malinkiewicz, O.; Yella, A.; Lee, Y. H.; Espallargas, G. M.; Graetzel, M.; Nazeeruddin, M. K.; Bolink, H. J. Perovskite Solar Cells Employing Organic Charge-Transport Layers. *Nat. Photonics* **2014**, *8*, 128–132.
- (16) Nie, W. Y.; Tsai, H. H.; Asadpour, R.; Blancon, J. C.; Neukirch, A. J.; Gupta, G.; Crochet, J. J.; Chhowalla, M.; Tretiak, S.; Alam, M. A.; et al. High-Efficiency Solution-Processed Perovskite Solar Cells with Millimeter-Scale Grains. *Science* **2015**, *347*, 522–525.
- (17) Bi, D. Q.; Boschloo, G.; Schwarzmüller, S.; Yang, L.; Johansson, E. M. J.; Hagfeldt, A. Efficient and Stable $\text{CH}_3\text{NH}_3\text{PbI}_3$ -Sensitized ZnO Nanorod Array Solid-State Solar Cells. *Nanoscale* **2013**, *5*, 11686–11691.
- (18) Kumar, M. H.; Yantara, N.; Dharani, S.; Grätzel, M.; Mhaisalkar, S.; Boix, P. P.; Mathews, N. Flexible, Low-Temperature, Solution Processed ZnO-Based Perovskite Solid State Solar Cells. *Chem. Commun.* **2013**, *49*, 11089–11091.
- (19) Juarez-Perez, E. J.; Wussler, M.; Fabregat-Santiago, F.; Lakus-Wollny, K.; Mankel, E.; Mayer, T.; Jaegermann, W.; Mora-Sero, I. Role of the Selective Contacts in the Performance of Lead Halide Perovskite Solar Cells. *J. Phys. Chem. Lett.* **2014**, *5*, 680–685.
- (20) Liu, D.; Kelly, T. L. Perovskite Solar Cells with a Planar Heterojunction Structure Prepared Using Room-Temperature Solution Processing Techniques. *Nat. Photonics* **2014**, *8*, 133–138.
- (21) Mahmood, K.; Swain, B. S.; Jung, H. S. Controlling the Surface Nanostructure of ZnO and Al-Doped ZnO Thin Films Using Electrostatic Spraying for their Application in 12% Efficient Perovskite Solar Cell. *Nanoscale* **2014**, *6*, 9127–9138.
- (22) Son, D. Y.; Im, J. H.; Kim, H. S.; Park, N. G. 11% Efficient Perovskite Solar Cell Based on ZnO Nanorods: An Effective Charge Collection System. *J. Phys. Chem. C* **2014**, *118*, 16567–16573.
- (23) Dong, J.; Zhao, Y.; Shi, J.; Wei, H.; Xiao, J.; Xu, L.; Luo, J.; Xu, J.; Li, Y.; Luo, Y.; et al. Impressive Enhancement in the Cell Performance of ZnO Nanorod-Based Perovskite Solar Cells with Al-Doped ZnO Interfacial Modification. *Chem. Commun.* **2014**, *50*, 13381–13384.
- (24) Liu, D.; Gangishetty, M. K.; Kelly, T. L. Effect of $\text{CH}_3\text{NH}_3\text{PbI}_3$ Thickness on Device Efficiency in Planar Heterojunction Perovskite Solar Cells. *J. Mater. Chem. A* **2014**, *2*, 19873.
- (25) Dong, X.; Hu, H.; Lin, B.; Ding, J.; Yuan, N. The Effect of ALD-ZnO Layers on the Formation of $\text{CH}_3\text{NH}_3\text{PbI}_3$ with Different Perovskite Precursors and Sintering. *Chem. Commun.* **2014**, *50*, 14405.
- (26) Pauporté, T.; Jouanno, E.; Pellé, F.; Viana, B.; Aschehoug, P. Key Growth Parameters for the Electrodeposition of ZnO Films with an Intense UV-Light Emission at Room Temperature. *J. Phys. Chem. C* **2009**, *113*, 10422.
- (27) Pauporté, T.; Jirka, I. Electrochemical Growth of Homogeneous Nanocrystalline ZnO Thin Films at Room Temperature. *Electrochim. Acta* **2009**, *54*, 7558–7564.
- (28) Liu, B.; Zeng, H. C. Hydrothermal Synthesis of ZnO Nanorods in the Diameter Regime of 50 nm. *J. Am. Chem. Soc.* **2003**, *125*, 4430.
- (29) Magne, C.; Moehl, T.; Urien, M.; Grätzel, M.; Pauporté, T. Effects of ZnO Film Growth Route and Nanostructure on Electron Transport and Recombination in Dye-Sensitized Solar Cells. *J. Mater. Chem. A* **2013**, *1*, 2079–2088.
- (30) Law, M.; Greene, L. E.; Johnson, J. C.; Saykally, R.; Yang, P. D. Nanowire Dye-Sensitized Solar Cells. *Nat. Mater.* **2005**, *4*, 455–459.
- (31) Izaki, M.; Omi, T. Transparent Zinc Oxide Films Prepared by Electrochemical Reaction. *Appl. Phys. Lett.* **1996**, *68*, 2439–2440.
- (32) Izaki, M.; Omi, T. Electrolyte Optimization for Cathodic Growth of Zinc Oxide Films. *J. Electrochem. Soc.* **1996**, *143*, L53–L55.
- (33) Lupon, O.; Pauporté, T.; Chow, L.; Viana, B.; Pellé, F.; Roldan Cuenya, B.; Ono, L. K.; Heinrich, H. Effects of Annealing on Properties of ZnO Thin Films Prepared by Electrochemical Deposition in Chloride Medium. *Appl. Surf. Sci.* **2010**, *256*, 1895–1907.
- (34) Cusco, R.; Alarcon-Llado, E.; Ibanez, J.; Artus, L.; Jimenez, J.; Wang, B. G.; Callahan, M. J. Temperature Dependence of Raman Scattering in ZnO. *Phys. Rev. B* **2007**, *75*, 165202.
- (35) Ohsaka, T.; Izumi, F.; Fujiki, Y. Raman Spectrum of Anatase, TiO_2 . *J. Raman Spectrosc.* **1978**, *7*, 321–324.
- (36) Juarez-Perez, E. J.; Wussler, M.; Fabregat-Santiago, F.; Lakus-Wollny, K.; Mankel, E.; Mayer, T.; Jaegermann, W.; Mora-Sero, I. Role of the Selective Contacts in the Performance of Lead Halide Perovskite Solar Cells. *J. Phys. Chem. Lett.* **2014**, *5*, 680–685.
- (37) Bisquert, J.; Bertoluzzi, L.; Mora-Sero, I.; Garcia-Belmonte, G. Theory of Impedance and Capacitance Spectroscopy of Solar Cells with Dielectric Relaxation, Drift-Diffusion Transport, and Recombination. *J. Chem. Phys. C* **2014**, *118*, 18983–18991.
- (38) Suarez, B.; Gonzalez-Pedro, V.; Ripolles, T. S.; Sanchez, R. S.; Otero, L.; Mora-Sero, I. Recombination Study of Combined Halides (Cl , Br , I) Perovskite Solar Cells. *J. Chem. Phys. Lett.* **2014**, *5*, 1628–1635.